A&A 603, A22 (2017)
DOI: 10.1051/0004-6361/201630210

Astronomy & Astrophysics

^{15}N fractionation in infrared-dark cloud cores⋆

S. Zeng[1], I. Jiménez-Serra[1], G. Cosentino[2], S. Viti[2], A. T. Barnes[3,4], J. D. Henshaw[3], P. Caselli[4], F. Fontani[5], and P. Hily-Blant[6]

[1] School of Physics and Astronomy, Queen Mary University of London, Mile End Road, E1 4NS London, UK
e-mail: z.shaoshan@qmul.ac.uk
[2] University College London, 132 Hampstead Road, London, NW1 2PS, UK
[3] Astrophysics Research Institute, Liverpool John Moores University, Liverpool, L3 5RF, UK
[4] Max-Planck Institute for Extraterrestrial Physics, Giessenbachstrasse 1, 85748 Garching, Germany
[5] INAF–Osservatorio Astrofisico di Arcetri, Largo E. Fermi 5, 50125 Firenze, Italy
[6] Institut de Planétologie et d'Astrophysique de Grenoble, 414 rue de la Piscine, 38041 Grenoble, France

Received 7 December 2016 / Accepted 19 May 2017

ABSTRACT

Context. Nitrogen is one of the most abundant elements in the Universe and its ^{14}N/^{15}N isotopic ratio has the potential to provide information about the initial environment in which our Sun formed. Recent findings suggest that the solar system may have formed in a massive cluster since the presence of short-lived radioisotopes in meteorites can only be explained by the influence of a supernova.
Aims. We seek to determine the ^{14}N/^{15}N ratio towards a sample of cold and dense cores at the initial stages in their evolution.
Methods. We observed the $J = 1 \rightarrow 0$ transitions of HCN, H^{13}CN, HC^{15}N, HN^{13}C, and H^{15}NC towards a sample of 22 cores in four infrared-dark clouds (IRDCs) which are believed to be the precursors of high-mass stars and star clusters. Assuming LTE and a temperature of 15 K, the column densities of HCN, H^{13}CN, HC^{15}N, HN^{13}C, and H^{15}NC are calculated and their ^{14}N/^{15}N ratio is determined for each core.
Results. The ^{14}N/^{15}N ratios measured in our sample of IRDC cores range between ∼70 and ≥763 in HCN and between ∼161 and ∼541 in HNC. These ratios are consistent with the terrestrial atmosphere (TA) and protosolar nebula (PSN) values, and with the ratios measured in low-mass prestellar cores. However, the ^{14}N/^{15}N ratios measured in cores C1, C3, F1, F2, and G2 do not agree with the results from similar studies towards the same cores using nitrogen bearing molecules with nitrile functional group (-CN) and nitrogen hydrides (-NH) although the ratio spread covers a similar range.
Conclusions. Relatively low ^{14}N/^{15}N ratios amongst the four-IRDCs were measured in IRDC G which are comparable to those measured in small cosmomaterials and protoplanetary disks. The low average gas density of this cloud suggests that the gas density, rather than the gas temperature, may be the dominant parameter influencing the initial nitrogen isotopic composition in young PSN.

Key words. ISM: molecules – astrochemistry – stars: formation

1. Introduction

For decades, our solar system was believed to have resided in a relatively isolated, low-mass molecular cloud core during its formation. However the detection of short-lived radioactive species in meteorites have suggested a different scenario in which the birthplace of the Sun may have been a massive cluster affected by a supernova event (Adams 2010; Dukes & Krumholz 2012; Pfalzner 2013; Nicholson & Parker 2017). If so, the initial chemical composition of our solar system, and thus of planets, meteorites and comets, may have been affected by the same physical process.

Measurements of the abundance isotopic ratios of the elements can be used to unveil the initial chemical composition of the protosolar nebulae (PSN) from which the solar system formed. The isotopic ratios of carbon (^{12}C/^{13}C) and oxygen (^{16}O/^{18}O) show a remarkable agreement among cometary materials, the local interstellar medium (ISM), and the solar value (Manfroid et al. 2009; Milam et al. 2005; Wilson & Rood 1994). Nitrogen, by contrast, has a peculiar behaviour since its ^{14}N/^{15}N isotopic ratio exhibits discrepancies across various environments within the solar system. The ^{14}N/^{15}N ratio measured in Jupiter's atmosphere (450 ± 100, Fouchet et al. 2004) is considered as the most representative value of the PSN and matches the present day solar wind value (441 ± 6, Marty et al. 2010). However, the ratios measured in the terrestrial atmosphere (TA; ∼272 in Earth, Junk & Svec 1958; 272 ± 54 in Venus, Hoffman et al. 1979; 173 ± 11 in Mars, Wong et al. 2013), comets (147.8 ± 5.7, Manfroid et al. 2009, 139 ± 26 from HCN and 165 ± 40 from CN, Bockelée-Morvan et al. 2008), interplanetary cust particles (or IDPs; values of 180−305; Floss et al. 2006) and meteorites (192−291, Alexander et al. 2007), are lower than those measured in Jupiter's atmosphere.

In molecular clouds, the discrepancies in the ^{14}N/^{15}N isotopic ratios spread over a larger range. In contrast to many molecular species (e.g. CO), N-bearing molecules do not suffer significant freeze-out onto grains in the coldest, densest regions of IRDCs, and are therefore reliable tracers of the gas chemistry and kinematics in cores. The nitrogen fractionation mechanisms are either due to chemical fractionation (Terzieva & Herbst 2000; Rodgers & Charnley 2008; Wirström et al. 2012; Hily-Blant et al. 2013) or a selective photodissociation effect (Lyons et al. 2009; Heays et al. 2014). Since IRDCs are dense and highly extinguished (with visual extinctions >10 mag; Kainulainen & Tan 2013), selective photodissociation

⋆ The reduced spectra (FITS files) are only available at the CDS via anonymous ftp to cdsarc.u-strasbg.fr (130.79.128.5) or via http://cdsarc.u-strasbg.fr/viz-bin/qcat?J/A+A/603/A22

is not expected to play an important role because this process becomes inefficient at $A_v \geq 3$ mag (Heays et al. 2014). As for chemical fractionation, these tracers can be categorized into: 1) hydride-bearing molecules with an amine (-NH) functional group believed to have originated from reactions with N_2; and 2) nitrile-bearing molecules with a nitrile (-CN) functional group that form via reactions with atomic N (Rodgers & Charnley 2008; Hily-Blant et al. 2013). Numerous measurements of the $^{14}N/^{15}N$ ratio exist towards low-mass prestellar cores (334 ± 50, 1000 ± 200 and 230 ± 90 from NH_3, N_2H^+ and HCN, respectively; Lis et al. 2010; Bizzocchi et al. 2013; Hily-Blant et al. 2013) and protostars (~160–290 from HCN and HNC; Wampfler et al. 2014), but observations of this ratio towards their massive counterparts are lacking.

A re-investigation of the fractionation processes of nitrogen in the ISM by Roueff et al. (2015) showed that nitrogen chemistry depends on the temperature and density of the primordial gas in the parental cloud. Since the Sun may have formed in a massive cluster, and low-mass and high-mass star-forming regions present gas temperatures and densities that differ by ~5–10 K and by factors of 10 (Pillai et al. 2006; Crapsi et al. 2007; Henshaw et al. 2013), measurements of the $^{14}N/^{15}N$ ratio in high-mass star-forming regions could provide insight into the initial bulk composition of the PSN.

Recently, Adande & Ziurys (2012) and Fontani et al. (2015) have measured the $^{14}N/^{15}N$ ratios towards a sample of high-mass star-forming regions. While in the Adande & Ziurys (2012) sample the $^{14}N/^{15}N$ ratios measured from CN and HNC lie between ~120–400, in the work of Fontani et al. (2015), these measurements range from ~180 to ~1300 in N_2H^+ and ~190 to ~450 in CN. In both studies, the $^{14}N/^{15}N$ ratios obtained from CN are comparable and fall between the TA and PSN values. However, only a few of these objects were prestellar in nature and larger samples of high-mass starless or prestellar cores are needed to measure the $^{14}N/^{15}N$ isotopic ratio in regions with physical conditions resembling those of the early stages of the solar system formation.

We present measurements of the $^{14}N/^{15}N$ isotopic ratio in HCN and HNC obtained towards a sample of 22 high-mass cold cores embedded in four IRDCs. These cores are believed to represent the nurseries of high-mass stars and star clusters and have physical properties (densities 10^4–10^6 cm^{-3} and temperatures ≤20 K; Pillai et al. 2006; Butler & Tan 2012) similar to those expected for the initial conditions of the solar system. In Sect. 2, we describe the observations and data analysis. The results are presented in Sect. 3.1 whilst the uncertainties involved in our calculations are discussed in Sect. 3.2. In Sects. 4.1–4.3 we investigate the correlation of IRDC cores with star formation activity and compare our results with previous measurements of the $^{14}N/^{15}N$ isotopic ratio in solar system objects along with low-mass and high-mass star-forming regions. In Sects. 4.4 and 4.5, we discuss the effects of ^{13}C depletion on the chemistry of nitrogen fractionation and the systematic trend observed in young and quiescent IRDCs with respect to more evolved, star-forming IRDCs. Our conclusions are presented in Sect. 5.

2. Observations

Observations of the $J = 1 \rightarrow 0$ rotational transition of HCN, $H^{13}CN$, $HC^{15}N$, $HN^{13}C$ and $H^{15}NC$ were obtained with the IRAM 30 m telescope[1] towards 22 massive cores embedded in IRDCs G028.37+00.07, G034.43+00.24, G034.77-00.55, and G035.39-00.33 (hereafter Clouds C, F, G and H respectively, as in Butler & Tan 2012). The frequencies of the transitions and molecular data are included in Table 1 whereas the properties of each IRDC are listed in Table 2. The EMIR receivers were tuned at 87 GHz and the FTS spectrometer provided a spectral resolution of 200 kHz (or ~0.68 km s^{-1}). The HNC($J = 1 \rightarrow 0$) transition was not covered within our frequency range. Typical system temperatures ranged from 106 K to 199 K. The half-power beam width (HPBW) of the telescope was 28″ at 87 GHz. The spectra were measured in units of antenna temperature, T_A^*, and converted into main beam temperature, T_{mb}, using a beam efficiency of 0.81. Data reduction was carried out using the GILDAS/CLASS software package[2]. The spectra of HCN ($J = 1 \rightarrow 0$), $H^{13}CN$($J = 1 \rightarrow 0$), $HC^{15}N$($J = 1 \rightarrow 0$), $HN^{13}C$($J = 1 \rightarrow 0$) and $H^{15}NC$($J = 1 \rightarrow 0$) were obtained towards all cores reported by Butler & Tan (2012) within Clouds F, G and H. For Cloud C, however, all cores were observed except C7 that laid outside our map. Thus C7 is not be considered in our analysis.

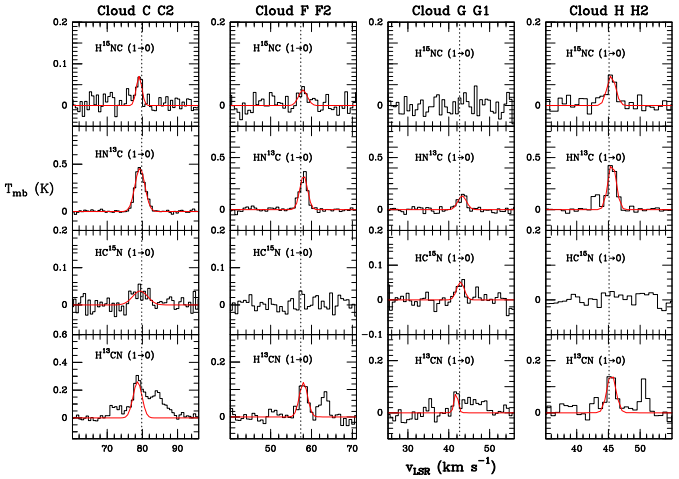

Fig. 1. *From left to right, top to bottom panels*: emission lines of $H^{15}NC$, $HN^{13}C$, $HC^{15}N$, and hyperfine transitions of $H^{13}CN$ observed with IRAM 30 m towards IRDCs C, F, G, and H. Red lines indicate the best Gaussian fit to the lines. The hyperfine components of $H^{13}CN$ were initially fitted but given the bad results of the fit; in a second step only the main $F = 2 \rightarrow 1$ component of $H^{13}CN$ was fitted using a single-Gaussian component profile (see red line in *bottom panels* and Sect. 3.1 for details). See also Figs. A.1–A.4 for all spectra taken.

Table 1. Observed HCN and HNC isotopologue transitions.

Molecules	Transition	Frequency [GHz]	A_{ul} [s^{-1}]	E_u [K]	g_u
$H^{13}CN$	$J = 1 \rightarrow 0$, $F = 1 \rightarrow 1$	86.33877	2.4×10^{-5}	4.14	3
$H^{13}CN$	$J = 1 \rightarrow 0$, $F = 2 \rightarrow 1$	86.34018	2.4×10^{-5}	4.14	5
$H^{13}CN$	$J = 1 \rightarrow 0$, $F = 0 \rightarrow 1$	86.34227	2.4×10^{-5}	4.14	1
$HC^{15}N$	$J = 1 \rightarrow 0$	86.05496	2.4×10^{-5}	4.13	3
$HN^{13}C$	$J = 1 \rightarrow 0$	87.09085	1.9×10		

Notes. Molecular data extracted from the JPL and CDMS molecular catalogues (Pickett et al. 1998; Müller et al. 2005).

3. Results

3.1. $^{14}N/^{15}N$ ratios derived from the ^{13}C isotopologues of HCN and HNC

In Fig. 1, we show a sample of spectra of $H^{13}CN$, $HC^{15}N$, $HN^{13}C$, and $H^{15}NC$ obtained towards one massive core in

[1] Based on observations carried out under projects number 134-12 and 027-13 with the IRAM 30 m Telescope. IRAM is supported by INSU/CNRS (France), MPG (Germany), and IGN (Spain).

[2] See http://www.iram.fr/IRAMFR/GILDAS

Table 2. Properties of IRDCs.

IRDCs	l [°]	b [°]	V_{LSR} [km s^{-1}]	Σ(sat) [g cm^{-2}]	M [$M_\odot$]	R_{gc} [kpc]	^{12}C/^{13}C
C(G028.37+00.07)	28.373	0.076	78.6	0.520	45 000	4.65	40.2
F(G034.43+00.24)	34.437	0.245	57.1	0.370	4460	5.74	46.8
G(G034.77-00.55)	34.771	–0.557	43.5	0.347	2010	6.24	49.8
H(G035.39-00.33)	35.395	–0.336	44.7	0.416	13 340	6.27	50.0

Notes. The table lists: Galactic coordinates l and b, average peak radial velocity V_{LSR}, mass surface density Σ(sat), mass M in solar mass (Butler & Tan 2012) and Galactocentric distance R_{gc}.

each IRDC; the rest of spectra are shown in the appendix in Figs. A.1−A.4. We assume that the emission from these isotopologues is optically thin and consider LTE conditions when calculating their column densities. For the excitation temperature T_{ex} of the molecular gas in these clouds, we assume a lower limit of 10 K and an upper limit of 20 K based on NH_3 measurements obtained towards other IRDCs (Pillai et al. 2006). Because the hyperfine structure of HN^{13}C cannot be resolved, we considered only one velocity component for this species, in the same way as for HC^{15}N and H^{15}NC. These lines were therefore fitted by using a single-component Gaussian profile. For H^{13}CN, the hyperfine structure of the $J = 1 \rightarrow 0$ transition could be resolved in the spectra and the HFS line fitting method implemented in CLASS was initially used to obtain the optical depth of the H^{13}CN emission.However, the HFS fits presented large uncertainties (see the optical depth values in Table A.5) and therefore, in a second step, we fitted the main $F = 2 \rightarrow 1$ component of H^{13}CN with a single-Gaussian component profile, calculated the column densities of H^{13}CN assuming optically thin emission, and corrected them by the statistical weight of the $F = 2 \rightarrow 1$ transition. The measured integrated intensities, radial velocities, line widths and peak intensities of the lines are listed in Tables A.1−A.4. We consider that a line is detected when its peak intensity is $\geq 3\sigma$ with σ the rms noise level measured in the spectra (see Col. 2 in Tables A.1−A.4). For the cores with no molecular detections, we used the 3σ noise level as upper limits to their peak intensities. If we take into account the optical depths derived from the HFS method (of ∼0.1−5.8), the resulting H^{13}CN column densities and hence the ^{14}N/^{15}N ratios are increased by factors of 3−6. Nevertheless, these values consistent with the previously determined results within the uncertainties.

The corresponding ^{14}N/^{15}N ratios were computed from the molecular column densities of the ^{14}N, ^{15}N HCN, and HNC isotopologues after correcting by the ^{12}C/^{13}C ratio for each IRDC. This ratio is calculated with the Galactic ^{12}C/^{13}C gradient as a function of Galactocentric distance derived by Milam et al. (2005) from CN measurements. The ^{12}C/^{13}C ratios for IRDCs C, F, G, and H are 40.2, 46.8, 49.8 and 50.0, respectively (see Table 2). The molecular column densities together with the derived ^{14}N/^{15}N ratios at T_{ex} = 15 K are listed in Table 3.

In our measurements, the uncertainties in the ^{14}N/^{15}N ratios were derived by propagating errors and using the 1σ uncertainties in the line integrated intensities calculated as rms $\times \sqrt{\Delta v \times \delta v}$, with Δv the average line width of the line for all cores with emission and with δv the velocity resolution of the spectrum (∼0.68 km s^{-1}). The derived uncertainties for the ^{14}N/^{15}N ratios are approximately ∼35%. This may due to the weak detection of molecules in some of the cores. For the cores with no detections, the ^{14}N/^{15}N ratios were estimated using the 3σ upper limits to the integrated intensities of H^{15}NC and HC^{15}N (see Col. 3 in Tables A.1−A.4), and they should be considered as lower limits.

Table 3. Column densities and nitrogen ratios obtained from the ^{13}C isotopologues of HCN and HNC.

	H^{13}CN	HC^{15}N	HN^{13}C	H^{15}NC	HCN	HNC
Core	$N_{tot}(T_{ex}$ = 15 K) [×10^{12} cm^{-2}]	$N_{tot}(T_{ex}$ = 15 K) [×10^{11} cm^{-2}]	$N_{tot}(T_{ex}$ = 15 K) [×10^{11} cm^{-2}]	$N_{tot}(T_{ex}$ = 15 K) [×10^{11} cm^{-2}]	^{14}N/^{15}N (T_{ex} = 15 K)	^{14}N/^{15}N (T_{ex} = 15 K)
			Cloud C			
C1	1.94	≤1.37	3.19	3.07	≥571 ± 65	418 ± 75
C2	3.03	4.09	4.25	3.57	298 ± 52	478 ± 63
C3	0.89	≤2.1	0.98	≤2.45	≥170 ± 64	≥161 ± 14
C4	2.02	4.20	3.42	5.07	193 ± 30	271 ± 31
C5	2.34	2.80	3.02	3.54	337 ± 89	342 ± 40
C6	1.92	2.26	2.44	2.34	343 ± 83	420 ± 82
C7	–	–	–	–	–	-
C8	1.23	≤1.33	1.94	2.41	≥371 ± 60	325 ± 73
C9	2.74	9.01	3.94	7.59	122 ± 20	209 ± 31
			Cloud F			
F1	1.82	≤1.12	2.05	3.99	≥763 ± 82	240 ± 26
F2	1.15	≤1.25	2.05	2.53	≥431 ± 63	378 ± 77
F3	1.11	1.51	2.25	1.95	346 ± 80	541 ± 79
F4	1.83	3.03	2.78	3.47	282 ± 60	374 ± 57
			Cloud G			
G1	0.35	2.47	0.92	≤1.94	70 ± 28	≥237 ± 21
G2	≤0.31	≤1.54	1.71	4.14	–	206 ± 31
G3	0.63	≤1.72	1.74	3.65	≥181 ± 54	237 ± 36
			Cloud H			
H1	0.98	≤1.39	1.91	4.09	≥353 ± 51	234 ± 20
H2	0.97	≤1.32	1.90	3.11	≥366 ± 132	306 ± 40
H3	1.84	2.00	2.19	2.24	458 ± 98	488 ± 68
H4	0.86	3.03	1.86	2.86	142 ± 34	326 ± 44
H5	1.13	1.44	1.96	2.96	395 ± 97	331 ± 36
H6	0.94	2.18	2.71	4.56	216 ± 77	297 ± 62

From Table 3, we find that the ^{14}N/^{15}N ratios obtained towards Clouds C, F, G, and H vary over a large range of values. In particular, for IRDCs C, F, and H, the nitrogen ratios in HCN range between 122–≥571, 282–≥763, and 142–458, respectively, while in HNC they range between ≥161−478 for Cloud C, 240–541 for Cloud F, and 234−488 for Cloud H. On the other hand, the ^{14}N/^{15}N ratios measured towards the cores in Cloud G are systematically lower ranging between 70–≥181 in HCN and 206–≥237 in HNC. We tested the effects of T_{ex} on our results, and found that if we use T_{ex} = 10 K or T_{ex} = 20 K instead of T_{ex} = 15 K, the derived ^{14}N/^{15}N isotopic ratios for both HCN and HNC do not vary significantly, lying within the ∼30% uncertainties. Higher T_{ex} (e.g. 50 K and 100 K) also confirm this behaviour, with the ^{14}N/^{15}N ratios changing within a factor of 1.2. Nevertheless, Roueff et al. (2015) have recently pointed out that species such as HN^{13}C and H^{13}CN may suffer significant depletion in molecular clouds, challenging the interpretation of ^{14}N/^{15}N isotopic ratios derived from ^{13}C containing isotopologues. In Sect. 3.2, we explore this possibility by directly measuring the ^{14}N/^{15}N ratios using HCN and its ^{15}N isotopologue towards the IRDCs cores in our sample with optically thin HCN emission.

3.2. ^{14}N/^{15}N ratios derived from HCN and its ^{15}N isotopologue

In this section, we test whether the ^{14}N/^{15}N ratios derived in Sect. 3.1 are significantly affected by ^{13}C depletion as proposed by the modelling of Roueff et al. (2015). We thus carried out direct measurements of the ^{14}N/^{15}N ratios with the $J = 1 \rightarrow 0$ rotational transitions of HCN and HC^{15}N, which were observed

Table 4. Column densities and nitrogen ratios obtained in HCN and its ^{12}C isotopologue.

	HCN	HC^{15}N	HCN
Core	$N_{tot}(T_{ex}$ = 15 K) [$\times 10^{13}$ cm^{-2}]	$N_{tot}(T_{ex}$ = 15 K) [$\times 10^{11}$ cm^{-2}]	^{14}N/^{15}N (T_{ex} = 15 K)
Cloud G			
G1	1.06	2.47	43 ± 9
G3	1.15	≤1.72	≥67 ± 3
Cloud H			
H2	3.72	≤1.32	≥282 ± 5
H3	5.26	2.00	263 ± 49
H4	3.65	3.03	121 ± 24
H5	3.71	1.44	259 ± 57

simultaneously within our frequency setup. HCN ($J = 1 \rightarrow 0$) is optically thick in IRDC star-forming cores such as the cores in Clouds C and F, or core H1 in Cloud H. Therefore for this test we only use the IRDC cores within our sample that show optically thin or moderately optically thick emission (i.e. with $\tau \lesssim 1-2$). These cores are G1 and G3 in Cloud G, and H2, H3, H4, and H5 in Cloud H. The rms noise level, integrated intensity, central radial velocity, line width, peak intensity, and derived optical depth of the HCN ($J = 1 \rightarrow 0$) lines, are shown in Table A.5 in the Appendix.

Following the same analysis procedures as for H^{13}CN in Sect. 3.1, the ^{14}N/^{15}N ratios were calculated from the column densities of HCN and HC^{15}N assuming optically thin emission, T_{ex} = 15 K, and LTE conditions (see Table 4). For the HC^{15}N non-detections, the upper limits to the column density of this molecule were estimated from the 3σ rms noise level in the HC^{15}N spectra. The derived ^{14}N/^{15}N ratios range from ≥67 to ≥282. If we compare these values with those from column 6 in Table 3, we find that the ^{14}N/^{15}N ratios inferred from HCN are systematically lower (by factors 1.2–2.7) with respect to those obtained from H^{13}CN. This is in contrast with the results from Roueff et al. (2015) since, from their models, the ^{12}C/^{13}C isotopic ratio measured from HCN should be a factor of ∼2 higher than that derived from CN (i.e. at timescales ≥1 Myr for the typical densities of IRDC cores of $\sim 10^5$ cm^{-3}; see Fig. 4 in their paper). This also holds if the ^{14}N/^{15}N ratios of the moderately optically thick cores are corrected by their HCN optical depths (with τ(HCN) = 0.71–1.84, which corresponds to correction factors of ∼1.4–2.2). Except for core H5, the corrected values of the ^{14}N/^{15}N ratios for cores H2, H3, and H4 are ≥503, 445 and 168, respectively, which are consistent with those inferred from H^{13}CN and lie within the uncertainties. Although our subsample of optically thin and moderately optically thick IRDC cores is small, this test suggests that the ^{14}N/^{15}N ratios obtained with the ^{13}C containing isotopologues are not strongly affected by ^{13}C depletion as proposed by the models of Roueff et al. (2015). In Sect. 4.5, we discuss the possible reasons for this.

4. Discussion

4.1. Correlation with star formation activity

The chemistry of HCN and HNC is known to be temperature dependent (Pineau des Forets et al. 1990) and any star formation activity in the core could locally heat the molecular gas enhancing the abundance of HCN (and its isotopologues) over HNC. Therefore, it is important to investigate whether the measured ^{14}N/^{15}N isotopic ratios in HCN and HNC show any correlation with the level of star formation activity in the observed IRDC cores. For this purpose, we adopted the classification of the embedded cores in IRDCs C, F, G and H proposed by Chambers et al. (2009) and Rathborne et al. (2010). Each of the cores is classified as quiescent, intermediate or active based upon their colour in *Spitzer*/IRAC 3–8 μm images as well as the presence or absence of 24 μm point source emission. The summary of the classification of each core is listed in Table 5.

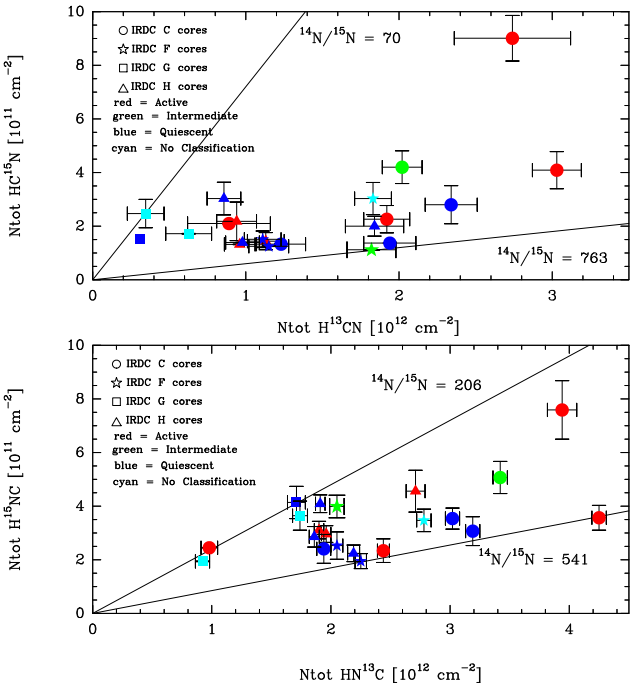

Fig. 2. Column densities of HCN (*top panel*) and HNC (*bottom panel*) ^{15}N isotopologues plotted against those of the ^{14}N species for all the cores in the sample. The cores are classified as active (red), intermediate (green), and quiescent (blue). Black indicates cores with no known classification. Different symbols are used to denote different clouds: IRDC C (circle), IRDC F(star), IRDC G (square), and IRDC H (triangle). The straight lines indicate the lowest and highest value of the corresponding ^{14}N/^{15}N ratio for each molecule.

We report the column densities of the ^{15}N isotopologues against those of the ^{14}N species in relation to their star formation classification in Fig. 2. This figure shows that there is no correlation between the column densities of the HCN or HNC isotopologues with the level of star formation activity in the IRDC cores. Such a conclusion is also confirmed by plotting the column densities of HC^{15}N against that of H^{15}NC. In other words, the measurements of ^{14}N/^{15}N ratio toward IRDCs C, F, G, and H from the $J = 1 \rightarrow 0$ transitions of HCN and HNC indeed probe the chemical composition of the envelope of these IRDCs cores. As such, it is in general not affected by local star formation feedback, although the highest ^{15}N/^{14}N ratio is found towards one of the active cores. Therefore, we cannot rule out that higher-J transitions and higher angular resolution observations give ^{15}N/^{14}N ratios that are correlated with star formation activity.

4.2. Comparison with solar system objects and low-mass star-forming regions

To understand whether IRDC cores have a nitrogen chemical composition that is consistent with that of the birthplace of the solar system, it is essential to compare the results obtained towards our sample of IRDC cores with those measured in solar system objects (see Fig. 3). For completeness, Fig. 3 also reports the ^{14}N/^{15}N ratios obtained towards low-mass prestellar or starless and star-forming cores. Overall, the ^{14}N/^{15}N ratios

Table 5. Summary of IRDC cores classification.

IRAC 3−8 μm	24 μm emission	Core category	Cores in IRDCs C, F, G and H
8.0μm	Yes/no	Red	–
Green Fuzzy	Yes	Active	C2, C3, C6, C9, H2, H5, H6
Green Fuzzy	No	Intermediate	C4, F1
None	Yes	–	–
None	No	Quiescent	C1, C5, C8, F2, F3, G2, H1, H3, H4
3.6 μm emission	Yes/no	Blue	–

Notes. Cores F4, G1 and G3 have not yet been classified (Rathborne et al. 2010; Chambers et al. 2009).

from Clouds C, F, and H show values that are similar to those observed in the Sun, planets, and prestellar or star-forming regions and consistent with the TA and the PSN values. On the other hand, the ^{14}N/^{15}N ratios measured towards Cloud G lie mostly at the level of the TA value and are significantly lower than the PSN value in Fig. 3. The results in Cloud G are also in agreement with the measurements obtained in comets, IDPs, meteorites, and especially protoplanetary disks (80−160) as recently measured by Guzmán et al. (2017). Furthermore, they marginally agree with the lower end of the ratios derived in starless or prestellar and star-forming cores. We also caution that half of the ^{14}N/^{15}N ratios in Cloud G are lower limits; HC^{15}N has not been detected in cores G2 and G3 and H^{15}NC has not been detected in core G1 (see Tables A.2 and A.4). Therefore we may be lacking enough statistics to draw a firm conclusion.

4.3. Comparison with high-mass star-forming regions

The comparison with the measurements from Adande & Ziurys (2012) and Fontani et al. (2015) towards high-mass star-forming regions, shows that our measurements are consistent with their results as a whole. Especially, the ^{14}N/^{15}N ratios from HNC in IRDCs almost lie in the same range as those measured by Adande & Ziurys (2012) in CN and HNC and by Fontani et al. (2015) in CN. The ^{14}N/^{15}N ratios from HCN are also compatible with the results measured by Fontani et al. (2015) in N_2H^+ emission. Since Fontani et al. (2015) also measured the ^{14}N/^{15}N ratio towards cores C1, F1, F2, and G2 included in our sample, we compared the results between each individual core and they show some discrepancies as a result. Indeed, the ^{14}N/^{15}N ratios obtained by Fontani et al. (2015) in N^{15}NH$^+$ and ^{15}NNH$^+$ (CN was not detected towards these cores) are ∼1445 and ∼1217 for C1, ∼672 and ∼566 for F1, and ∼872 and ∼856 for G2, respectively, i.e. overall significantly higher than those measured in this work. In contrast, F2 shows a lower value of ∼232 and ≥195 in ^{15}NNH$^+$ and N^{15}NH$^+$, respectively. These large discrepancies have also been found in low-mass prestellar cores and could be associated with the different chemistries involved in the formation of N_2H^+ and HNC/HCN (Wirström et al. 2012; Hily-Blant et al. 2013; Bizzocchi et al. 2013). More recently, cores C1, C3, F1, F2 and G2 have been studied independently by Colzi et al. (2017) using isotopologues of HCN and HNC. A similar range for the ^{14}N/^{15}N ratios has been found in HCN (≥150−748) whilst results in HNC lie in a slightly higher range (263−813). In both samples, core G2 shows one of the smallest ratios in HCN and HNC.

4.4. ^{13}C depletion and its effects on nitrogen fractionation

We evaluated whether the depletion of ^{13}C for species such (as HCN and HNC as predicted by the models of Roueff et al. 2015) could affect our derived values of the ^{14}N/^{15}N ratios in Sect. 3.2. Our test revealed that the ^{14}N/^{15}N values inferred from HCN are either consistent, or lower, than those measured from the ^{13}C isotopologue, in contrast to the modelling predictions. This could be due to two reasons: first, the timescales (age) of IRDC cores and, second the kinetic temperature of the gas within them.

Regarding the timescales, Kong et al. (2017) have modelled the chemistry of deuterated species such as N_2D^+ in IRDC cores to provide constraints to the dynamical age of these cores. Their modelling shows that the enhanced D/H ratio in these objects can be reproduced for timescales of ∼10^5 yr; these authors model the N_2D^+ emission arising from the C1 core in Cloud C. On the other hand, Roueff et al. (2015) predict similar ^{12}C/^{13}C ratios associated with CN and with HCN/HNC at these timescales (of ∼10^5 yr) for the typical H_2 gas densities of IRDC cores (of ∼10^5 cm^{-3}; see Butler & Tan 2012). The large differences in ^{12}C/^{13}C ratios associated with HCN/HNC, such as those discussed in Sect. 3.2, would therefore not be expected.

Nevertheless, the definition of a core formation timescale is somewhat ambiguous, for example Barnes et al. (2016) found that the D/H fraction within Cloud F would have taken several 10^6 yr to form. In light of this, a more self-consistent comparison between timescales inferred by chemical models is required.

Concerning the gas temperature of IRDC cores, measurements of the emission of NH_3 towards these cores give kinetic temperatures of the gas of 15−20 K (Pillai et al. 2006), which are higher than those assumed in the models of Roueff et al. (2015, of 10 K). Since carbon depletion is strongly dependent on gas/dust temperature, it is unclear whether these results can be compared directly to IRDC cores; there are no models are provided for temperatures higher than 10 K. Therefore, additional modelling is needed to test the effects of ^{13}C depletion in the chemistry of nitrogen fractionation at slightly higher temperatures similar to those found in IRDCs.

4.5. Systematic trend of ^{14}N/^{15}N ratio between IRDCs

Table 3 and Fig. 3 show that the ^{14}N/^{15}N ratios observed in Cloud G are systematically lower than those measured in Clouds C, F and H. This may be due to the properties of Cloud G itself. As discussed in Sect. 4.1, cores G1, G2 and G3 do not show any trace of star formation activity, whilst the other three IRDCs show several cores that are actively forming stars (see e.g. cores C2 or H2). In addition, Cloud G is the least massive, the most diffuse (it has the weakest emission in high-density tracers; Cosentino et al., in prep.), and has the lowest peak H_2 mass surface density amongst the four targeted IRDCs (see Table 2 and Butler & Tan 2012). Given that the kinetic temperature of the gas is similar across IRDCs (∼15−20 K), we propose that density could be one of the important parameters that is responsible for the discrepancies found between Cloud G and the other

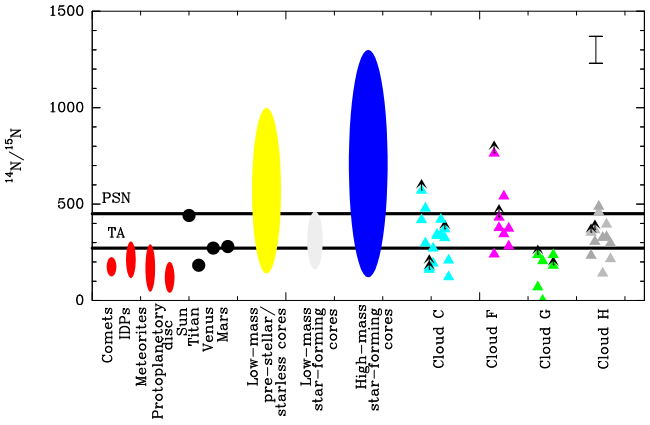

Fig. 3. Nitrogen isotope ratio variations measured in different sources starting from small solar system bodies (in red; Busemann et al. 2006; Floss et al. 2006; Alexander et al. 2007; Bockelée-Morvan et al. 2008; Manfroid et al. 2009; Mumma & Charnley 2011; Guzmán et al. 2017) to planets (in black; Junk & Svec 1958; Hoffman et al. 1979; Fouchet et al. 2004; Niemann et al. 2005; Marty et al. 2010; Wong et al. 2013; Fletcher et al. 2014), low-mass prestellar cores (in yellow; Gerin et al. 2009; Bizzocchi et al. 2010; Lis et al. 2010; Bizzocchi et al. 2013; Hily-Blant et al. 2013), low-mass star-forming cores (in light grey; Wampfler et al. 2014) and high-mass star-forming cores (in blue; Adande & Ziurys 2012; Fontani et al. 2015). Our measurements in IRDCs are shown on the right. On the upper right corner, we show a representative error bar for our measurements of the $^{14}N/^{15}N$ ratio. Black arrows indicate the lower limits in our measurements. The $^{14}N/^{15}N$ ratio measured in HCN from core G2 is shown as zero with no lower limit indication owing to both of the column densities of $H^{13}CN$ and $HC^{15}N$ are only given as upper limits.

IRDCs, although the models do not agree with this scenario. Therefore, we speculate that the PSN may have formed in an IRDC with properties similar to those of cloud G. However, the properties of this sample of IRDC cores need to be further investigated along with relevant chemical models to confirm the proposed idea.

5. Conclusions

We have measured the nitrogen isotopic ratio $^{14}N/^{15}N$ towards a sample of cold IRDC cores. This ratio ranges between ~70 and ≥763 in HCN and between ~161 and ~541 in HNC. In particular, Cloud G systematically shows lower nitrogen isotopic ratios than the other three clouds, where values are consistent with the ratio measured towards small solar system bodies such as comets, IDPs, meteorites and also proto-planetary disks. Since Cloud G shows lower overall gas densities, and since it likely is at an earliest stage of evolution, we propose that gas density is the key parameter in nitrogen fractionation in IRDCs. Higher angular resolution observations, as well as chemical modelling of the nitrogen fractionation of HCN and HNC at temperatures similar to those found in IRDCs, are needed to establish the origin of the discrepancies in the measured $^{14}N/^{15}N$ ratios found in Cloud G with respect to Clouds C, F and H. The comparison between the modeling predictions and our IRDC measurements may allow us to constrain the main chemical reactions involved in the fractionation process of nitrogen in the protosolar nebula.

Acknowledgements. We would like to thank Audrey Coutens and the anonymous referee for valuable comments to a previous version of the manuscript. I.J.-S. acknowledges the financial support received from the STFC through an Ernest Rutherford Fellowship (proposal number ST/L004801/2). P.C. acknowledges financial support of the European Research Council (ERC; project PALs 320620). The research leading to these results has also received funding from the European Commission (FP/2007−2013) under grant agreement No. 283393 (RadioNet3).

References

Adams, F. C. 2010, ARA&A, 48, 47
Adande, G. R., & Ziurys, L. M. 2012, ApJ, 744, 194
Alexander, C. M. O. D., Fogel, M., Yabuta, H., & Cody, G. D. 2007, Geochim. Cosmochim. Acta, 71, 4380
Barnes, A. T., Kong, S., Tan, J. C., et al. 2016, MNRAS, 458, 1990
Bizzocchi, L., Caselli, P., & Dore, L. 2010, A&A, 510, L5
Bizzocchi, L., Caselli, P., Leonardo, E., & Dore, L. 2013, A&A, 555, A109
Bockelée-Morvan, D., Biver, N., Jehin, E., et al. 2008, ApJ, 679, L49
Busemann, H., Young, A. F., O'D. Alexander, C. M., et al. 2006, Science, 312, 727
Butler, M. J., & Tan, J. C. 2012, ApJ, 754, 5
Chambers, E. T., Jackson, J. M., Rathborne, J. M., & Simon, R. 2009, ApJS, 181, 360
Colzi, L., Fontani, F., Caselli, P., et al. 2017, A&A, submitted
Crapsi, A., Caselli, P., Walmsley, M. C., & Tafalla, M. 2007, A&A, 470, 221
Dukes, D., & Krumholz, M. R. 2012, ApJ, 754, 56
Fletcher, L. N., Greathouse, T. K., Orton, G. S., et al. 2014, Icarus, 238, 170
Floss, C., Stadermann, F. J., Bradley, J. P., et al. 2006, Geochim. Cosmochim. Acta, 70, 2371
Fontani, F., Caselli, P., Palau, A., Bizzocchi, L., & Ceccarelli, C. 2015, ApJ, 808, L46
Fouchet, T., Irwin, P. G. J., Parrish, P., et al. 2004, Icarus, 172, 50
Gerin, M., Marcelino, N., Biver, N., et al. 2009, A&A, 498, L9
Guzmán, V. V., Öberg, K. I., Huang, J., Loomis, R., & Qi, C. 2017, ApJ, 836, 30
Heays, A., van Dishoeck, E., Visser, R., et al. 2014, in 69th International Symposium on Molecular Spectroscopy
Henshaw, J. D., Caselli, P., Fontani, F., et al. 2013, MNRAS, 428, 3425
Hily-Blant, P., Bonal, L., Faure, A., & Quirico, E. 2013, Icarus, 223, 582
Hoffman, J. H., Hodges, R. R., McElroy, M. B., Donahue, T. M., & Kolpin, M. 1979, Science, 205, 49
Junk, G., & Svec, H. J. 1958, Geochim. Cosmochim. Acta, 14, 234
Kainulainen, J., & Tan, J. C. 2013, A&A, 549, A53
Kong, S., Tan, J. C., Caselli, P., et al. 2017, ApJ, submitted [arXiv:1701.05953]
Lis, D. C., Wootten, A., Gerin, M., & Roueff, E. 2010, ApJ, 710, L49
Lyons, J. R., Bergin, E. A., Ciesla, F. J., et al. 2009, Geochim. Cosmochim. Acta, 73, 4998
Manfroid, J., Jehin, E., Hutsemékers, D., et al. 2009, A&A, 503, 613
Marty, B., Zimmermann, L., Burnard, P. G., et al. 2010, Geochim. Cosmochim. Acta, 74, 340
Milam, S. N., Savage, C., Brewster, M. A., Ziurys, L. M., & Wyckoff, S. 2005, ApJ, 634, 1126
Müller, H. S. P., Schlöder, F., Stutzki, J., & Winnewisser, G. 2005, J. Mol. Struct., 742, 215
Mumma, M. J., & Charnley, S. B. 2011, ARA&A, 49, 471
Nicholson, R. B., & Parker, R. J. 2017, MNRAS, 464, 4318
Niemann, H. B., Atreya, S. K., Bauer, S. J., et al. 2005, Nature, 438, 779
Pfalzner, S. 2013, A&A, 549, A82
Pickett, H. M., Poynter, R. L., Cohen, E. A., et al. 1998, J. Quant. Spectr. Rad. Transf., 60, 883
Pillai, T., Wyrowski, F., Carey, S. J., & Menten, K. M. 2006, A&A, 450, 569
Pineau des Forets, G., Roueff, E., & Flower, D. R. 1990, MNRAS, 244, 668
Rathborne, J. M., Jackson, J. M., Chambers, E. T., et al. 2010, ApJ, 715, 310
Rodgers, S. D., & Charnley, S. B. 2008, ApJ, 689, 1448
Roueff, E., Loison, J. C., & Hickson, K. M. 2015, A&A, 576, A99
Terzieva, R., & Herbst, E. 2000, MNRAS, 317, 563
Wampfler, S. F., Jørgensen, J. K., Bizzarro, M., & Bisschop, S. E. 2014, A&A, 572, A24
Wilson, T. L., & Rood, R. 1994, ARA&A, 32, 191
Wirström, E. S., Charnley, S. B., Cordiner, M. A., & Milam, S. N. 2012, ApJ, 757, L11
Wong, M. H., Atreya, S. K., Mahaffy, P. N., et al. 2013, Geophys. Res. Lett., 40, 6033

Appendix A: Spectra and fitting parameters of isotopologues of HCN and HNC

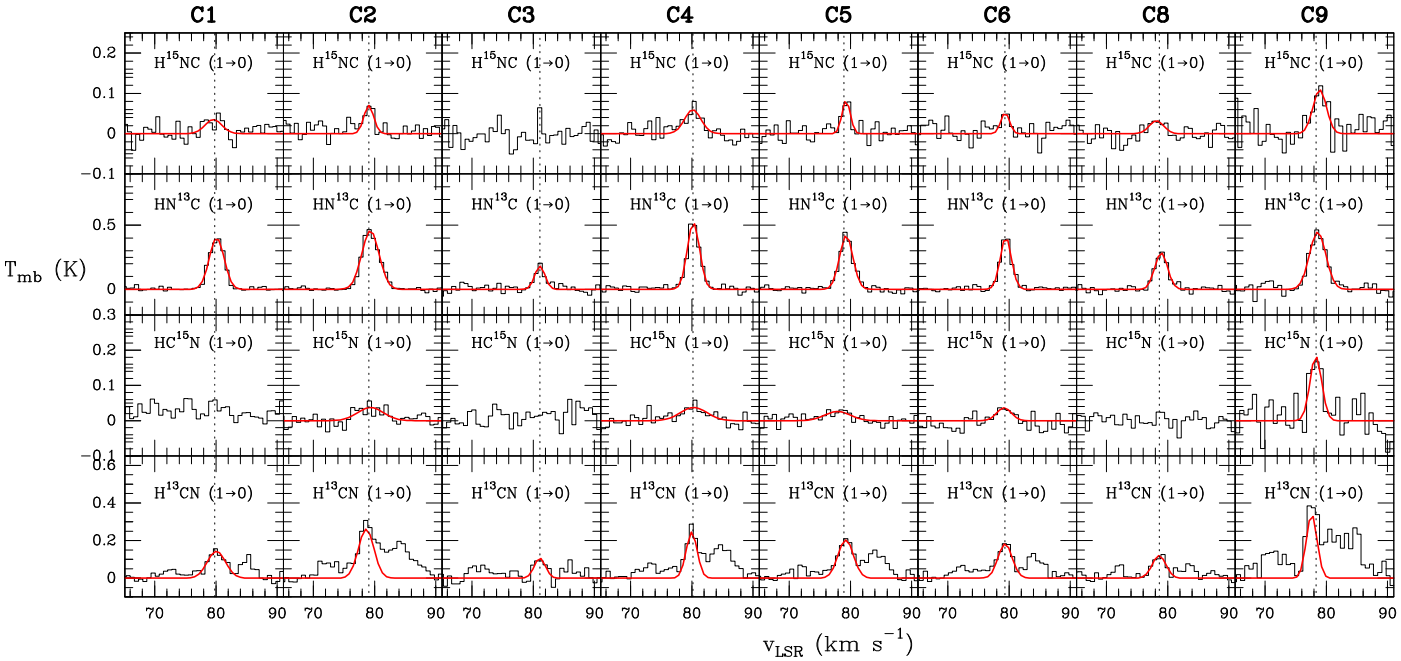

Fig. A.1. Spectra of HC^{15}N, HN^{13}C, H^{15}NC, and H^{13}CN observed with IRAM 30 m towards IRDC C. The red line indicates the best Gaussian fit. The hyperfine components of H^{13}CN were initially fitted but given the bad results of the fit, in a second step only the main $F = 2 \rightarrow 1$ component of H^{13}CN was fitted with a single-Gaussian component profile (see red line in bottom panels and Sect. 3.1 for details).

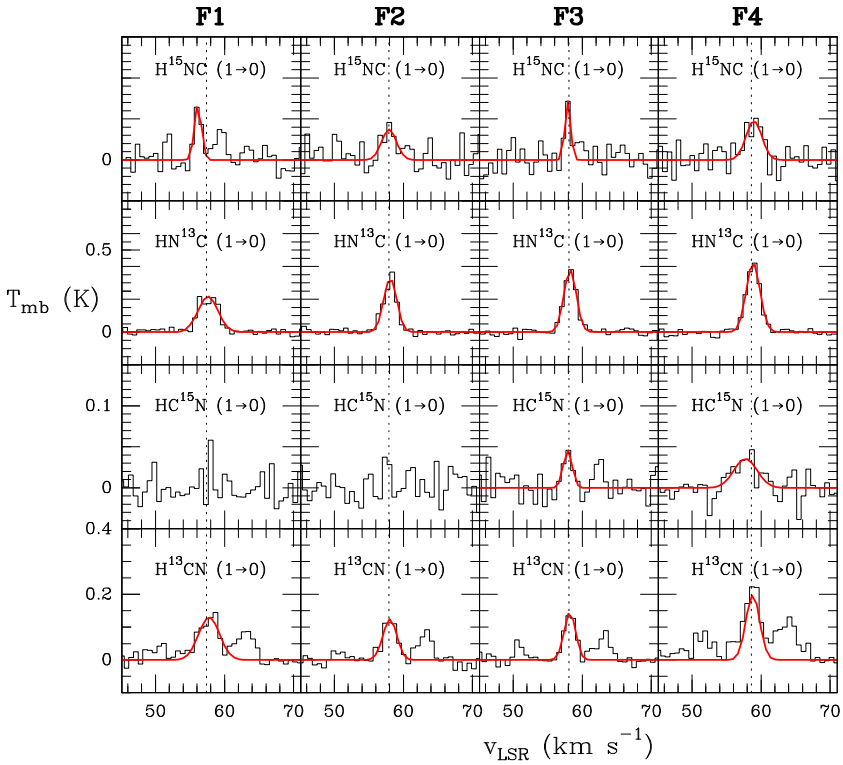

Fig. A.2. Spectra of HC^{15}N, HN^{13}C, H^{15}NC, and H^{13}CN observed with IRAM 30 m towards IRDC F. The red line indicates the best Gaussian fit. The hyperfine components of H^{13}CN were initially fitted but given the bad results of the fit, in a second step only the main $F = 2 \rightarrow 1$ component of H^{13}CN was fitted with a single-Gaussian component profile (see red line in bottom panels and Sect. 3.1 for details).

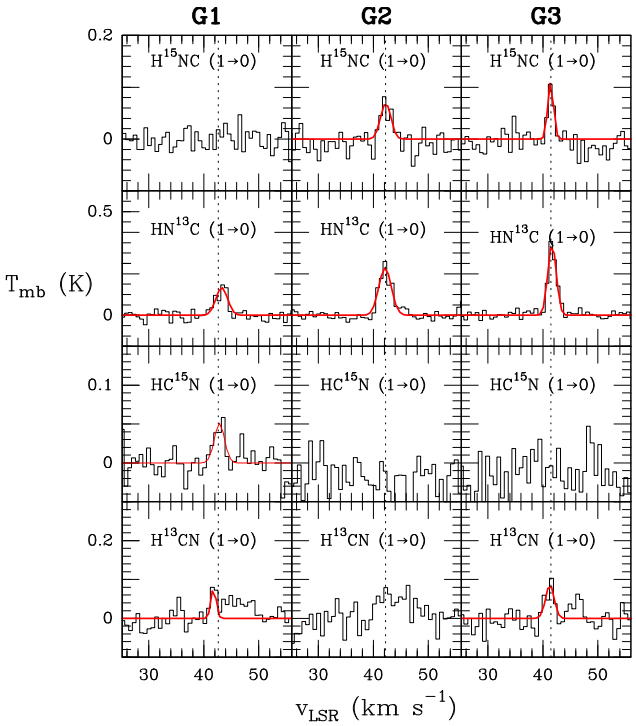

Fig. A.3. Spectra of $HC^{15}N$, $HN^{13}C$, $H^{15}NC$, and $H^{13}CN$ observed with IRAM 30 m towards IRDC G. Only the main component of $H^{13}CN$ was fitted with a single-Gaussian component profile, which was then used to calculate the column densities. The red line indicates the best Gaussian fit and these spectra were scaled to fit into each individual panel.

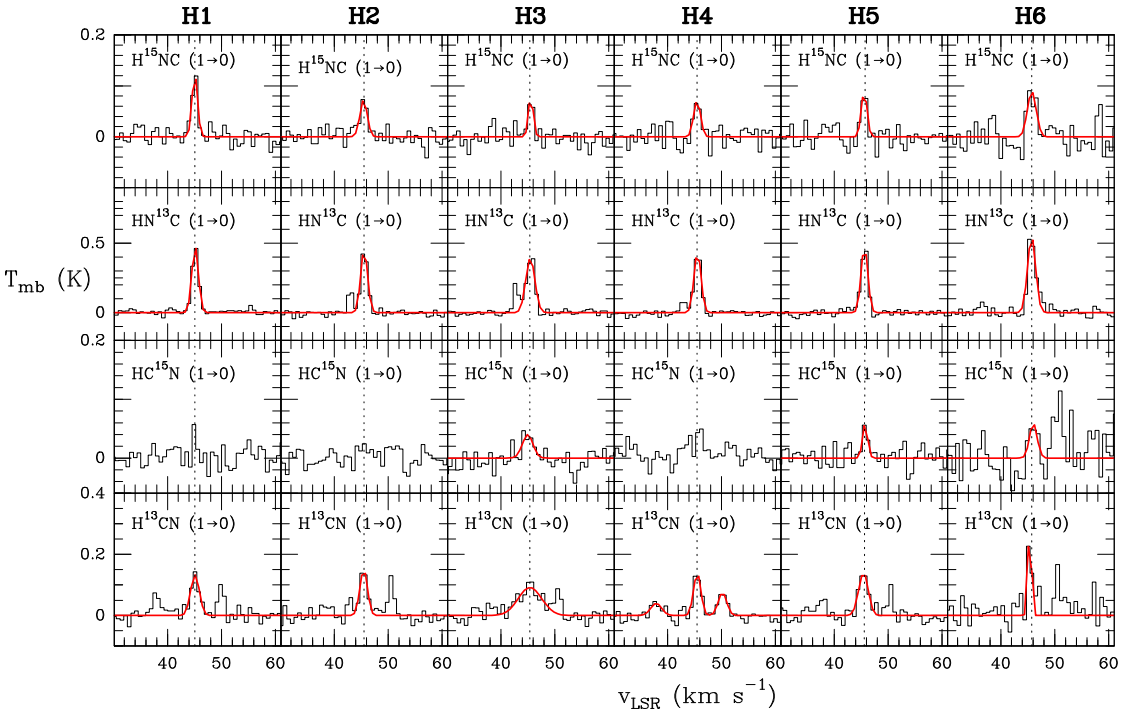

Fig. A.4. Spectra of $HC^{15}N$, $HN^{13}C$, $H^{15}NC$, and $H^{13}CN$ observed with IRAM 30 m towards IRDC H. The red line indicates the best Gaussian fit. The hyperfine components of $H^{13}CN$ were initially fitted but given the bad results of the fit, in a second step only the main $F = 2 \rightarrow 1$ component of $H^{13}CN$ was fitted with a single-Gaussian component profile (see red line in bottom panels and Sect. 3.1 for details).

Table A.1. Root mean square noise in the spectra rms, integrated intensities $\int T_{\rm mb} {\rm d}\upsilon$, radial velocity υ, line widths $\Delta\upsilon$, and peak temperature $T_{\rm peak}$ of HC^{15}N(1 → 0) in cores within Clouds C, F, G, and H.

Core	rms [10^{-2} K]	$\int T_{\rm mb}\Delta\upsilon$ [K km s^{-1}]	υ [km s^{-1}]	$\Delta\upsilon$ [km s^{-1}]	$T_{\rm peak}$ [K]
Cloud C					
C1*	1.8	≤0.07	–	–	≤0.05
C2	1.8	0.2 ± 0.05	79.36 ± 0.62	5.02 ± 1.07	0.04
C3*	2.7	≤0.10	–	–	≤0.08
C4	1.6	0.21 ± 0.05	80.31 ± 0.59	5.12 ± 1.71	0.04
C5	1.9	0.14 ± 0.05	77.89 ± 0.89	4.90 ± 2.16	0.03
C6	1.8	0.11 ± 0.04	79.19 ± 0.50	2.81 ± 1.01	0.04
C7	–	–	–	–	–
C8*	1.7	≤0.06	–	–	≤0.05
C9	3.3	0.44 ± 0.07	78.30 ± 0.17	2.26 ± 0.37	0.18
Cloud F					
F1*	1.5	≤0.05	–	–	≤0.04
F2*	1.6	≤0.06	–	–	≤0.05
F3	1.5	0.07 ± 0.02	57.9 ± 0.22	1.49 ± 0.49	0.05
F4	1.8	0.15 ± 0.04	57.74 ± 0.54	3.93 ± 1.05	0.04
Cloud G					
G1	2.1	0.12 ± 0.04	42.85 ± 0.35	2.20 ± 0.67	0.05
G2*	2.0	≤0.08	–	–	≤0.06
G3*	2.2	≤0.08	–	–	≤0.07
Cloud H					
H1*	1.8	≤0.07	–	–	≤0.05
H2*	1.7	≤0.06	–	–	≤0.05
H3	1.5	0.10 ± 0.03	44.97 ± 0.33	2.28 ± 0.86	0.04
H4	1.8	0.15 ± 0.04	45.37 ± 0.56	3.99 ± 1.17	0.03
H5	1.8	0.07 ± 0.02	45.74 ± 0.19	1.13 ± 0.48	0.06
H6	3.3	0.11 ± 0.05	46.03 ± 0.43	1.68 ± 0.63	0.06

Notes. (*) Indicates 3σ upper-limit values for $T_{\rm peak}$. ≤ on the integrated intensity $\int T_{\rm mb}\ \Delta\upsilon$ indicates the upper limits which are calculated as $3\sigma \times \sqrt{\delta\upsilon \times \Delta\upsilon}$ with $\delta\upsilon$ the spectral resolution (0.68 km s^{-1}) and $\Delta\upsilon$ the average line width measured considering all cores.

Table A.2. Root mean square noise in the spectra rms, integrated intensities $\int T_{\rm mb} {\rm d}\upsilon$, radial velocity υ, line widths $\Delta\upsilon$, and peak temperature $T_{\rm peak}$ of HN^{13}C(1→0) in cores within Clouds C, F, G, and H.

Core	rms [10^{-2} K]	$\int T_{\rm mb}\Delta\upsilon$ [K km s^{-1}]	υ [km s^{-1}]	$\Delta\upsilon$ [km s^{-1}]	$T_{\rm peak}$ [K]
Cloud C					
C1	1.8	1.22 ± 0.03	80.12 ± 0.04	2.84 ± 0.09	0.41
C2	1.7	1.62 ± 0.04	79.32 ± 0.04	3.32 ± 0.08	0.46
C3	2.3	0.37 ± 0.05	81.09 ± 0.11	1.93 ± 0.34	0.18
C4	1.6	1.30 ± 0.03	80.26 ± 0.03	2.35 ± 0.07	0.52
C5	1.6	1.15 ± 0.04	79.31 ± 0.04	2.57 ± 0.10	0.42
C6	1.7	0.93 ± 0.03	79.47 ± 0.04	2.15 ± 0.09	0.41
C7	–	–	–	–	–
C8	1.7	0.74 ± 0.04	78.94 ± 0.06	2.44 ± 0.14	0.29
C9	3.2	1.50 ± 0.07	78.59 ± 0.07	3.16 ± 0.17	0.45
Cloud F					
F1	1.5	0.78 ± 0.03	57.61 ± 0.07	3.39 ± 0.15	0.22
F2	1.6	0.78 ± 0.03	58.09 ± 0.04	2.22 ± 0.10	0.33
F3	1.5	0.86 ± 0.03	58.25 ± 0.04	2.12 ± 0.09	0.38
F4	1.7	1.06 ± 0.03	58.85 ± 0.04	2.35 ± 0.08	0.42
Cloud G					
G1	1.9	0.35 ± 0.04	43.28 ± 0.15	2.47 ± 0.34	0.13
G2	2.1	0.65 ± 0.04	42.15 ± 0.08	2.67 ± 0.19	0.23
G3	2.2	0.66 ± 0.03	41.68 ± 0.05	1.79 ± 0.11	0.35
Cloud H					
H1	1.7	0.73 ± 0.03	45.13 ± 0.02	1.43 ± 0.06	0.48
H2	1.6	0.73 ± 0.04	45.57 ± 0.03	1.50 ± 0.09	0.46
H3	1.6	0.84 ± 0.05	45.48 ± 0.06	2.00 ± 0.16	0.39
H4	1.6	0.71 ± 0.03	45.58 ± 0.03	1.53 ± 0.07	0.44
H5	1.7	0.75 ± 0.03	45.64 ± 0.03	1.46 ± 0.06	0.48
H6	2.8	1.03 ± 0.05	45.73 ± 0.04	1.77 ± 0.09	0.55

Table A.3. Root mean square noise in the spectra rms, integrated intensities $\int T_{\rm mb} d\upsilon$, radial velocity υ, line widths $\Delta\upsilon$, and peak temperature $T_{\rm peak}$ of $H^{15}NC(1 \rightarrow 0)$ in cores within Clouds C, F, G, and H.

Core	rms [10^{-2} K]	$\int T_{\rm mb}\Delta\upsilon$ [K km s^{-1}]	υ [km s^{-1}]	$\Delta\upsilon$ [km s^{-1}]	$T_{\rm peak}$ [K]
Cloud C					
C1	1.4	0.12 ± 0.03	79.58 ± 0.47	3.24 ± 0.72	0.04
C2	1.6	0.14 ± 0.03	79.06 ± 0.20	1.88 ± 0.57	0.07
C3*	2.6	≤0.10	–	–	≤0.07
C4	1.5	0.20 ± 0.04	80.16 ± 0.30	3.17 ± 0.85	0.06
C5	1.5	0.14 ± 0.02	79.30 ± 0.14	1.57 ± 0.32	0.08
C6	1.7	0.09 ± 0.03	79.37 ± 0.27	1.66 ± 0.79	0.05
C7	–	–	–	–	-
C8	1.5	0.10 ± 0.03	78.17 ± 0.47	2.76 ± 0.83	0.03
C9	3.3	0.30 ± 0.07	78.92 ± 0.27	2.58 ± 0.07	0.11
Cloud F					
F1	0.9	0.09 ± 0.02	56.14 ± 0.13	1.21 ± 0.30	0.03
F2	1.6	0.10 ± 0.03	57.92 ± 0.42	2.50 ± 1.12	0.04
F3	1.3	0.08 ± 0.02	57.90 ± 0.12	1.00 ± 0.21	0.07
F4	1.5	0.14 ± 0.03	58.95 ± 0.32	2.69 ± 0.61	0.05
Cloud G					
G1*	2.0	≤0.08	–	–	≤0.06
G2	1.9	0.16 ± 0.03	42.26 ± 0.26	2.22 ± 0.46	0.07
G3	2.3	0.14 ± 0.03	41.42 ± 0.13	1.24 ± 0.26	0.11
Cloud H					
H1	1.5	0.16 ± 0.02	45.05 ± 0.07	1.20 ± 0.22	0.13
H2	1.5	0.12 ± 0.03	45.44 ± 0.15	1.60 ± 0.51	0.07
H3	1.4	0.09 ± 0.02	45.56 ± 0.12	1.04 ± 0.37	0.08
H4	1.5	0.11 ± 0.02	45.49 ± 0.15	1.50 ± 0.21	0.07
H5	1.4	0.12 ± 0.02	45.57 ± 0.11	1.23 ± 0.26	0.09
H6	2.7	0.18 ± 0.04	45.75 ± 0.24	1.90 ± 0.38	0.09

Notes. (*) Indicates 3σ upper-limit values for $T_{\rm peak}$. ≤ on the integrated intensity $\int T_{\rm mb}\ \Delta\upsilon$ indicates the upper limits which are calculated as $3\sigma \times \sqrt{\delta\upsilon \times \Delta\upsilon}$ with $\delta\upsilon$ the spectral resolution (0.68 km s^{-1}) and $\Delta\upsilon$ the average line width measured considering all cores.

Table A.4. Root mean square noise in the spectra rms, integrated intensities $\int T_{\rm mb} d\upsilon$, radial velocity υ, line widths $\Delta\upsilon$, peak temperature $T_{\rm peak}$ of the $H^{13}CN$ ($1 \rightarrow 0$, $F = 2 \rightarrow 1$) hyperfine component and optical depth τ of the $H^{13}CN(1 \rightarrow 0)$ emission in cores within Clouds C, F, G, and H.

Core	rms [10^{-2} K]	$\int T_{\rm mb}\Delta\upsilon$ [K km s^{-1}]	υ [km s^{-1}]	$\Delta\upsilon$ [km s^{-1}]	$T_{\rm peak}$ [K]	τ
Cloud C						
C1	1.8	0.53 ± 0.05	80.08 ± 0.14	3.46 ± 0.39	0.14	1.47 ± 1.18
C2	1.8	0.83 ± 0.13	78.63 ± 0.10	2.97 ± 0.31	0.26	1.79 ± 0.57
C3	3.4	0.24 ± 0.06	81.08 ± 0.27	2.13 ± 0.46	0.11	2.86 ± 4.00
C4	1.6	0.55 ± 0.07	79.98 ± 0.07	2.11 ± 0.22	0.25	1.75 ± 0.63
C5	1.9	0.63 ± 0.07	79.24 ± 0.13	2.95 ± 0.35	0.20	1.33 ± 0.81
C6	1.7	0.52 ± 0.07	79.36 ± 0.12	2.69 ± 0.30	0.18	1.87 ± 1.00
C7	–	–	–	–	–	–
C8	1.8	0.33 ± 0.04	78.60 ± 0.15	2.61 ± 0.39	0.12	2.11 ± 2.09
C9	4.8	0/75 ± 0.15	77.62 ± 0.13	2.05 ± 0.29	0.34	5.88 ± 2.22
Cloud F						
F1	1.5	0.50 ± 0.04	57.77 ± 0.14	3.57 ± 0.40	0.13	2.29 ± 1.25
F2	1.6	0.31 ± 0.03	58.04 ± 0.11	2.36 ± 0.26	0.13	1.17 ± 1.43
F3	1.5	0.30 ± 0.03	58.21 ± 0.08	1.95 ± 0.18	0.15	1.32 ± 1.36
F4	1.5	0.50 ± 0.05	58.81 ± 0.07	2.36 ± 0.18	0.20	0.81 ± 0.66
Cloud G						
G1	2.1	0.09 ± 0.03	41.79 ± 0.16	1.11 ± 0.36	0.08	5.35 ± 5.78
G2*	2.2	≤0.08	–	–	≤0.07	0.1 ± 2.34
G3	2.0	0.17 ± 0.03	41.27 ± 0.20	1.84 ± 0.39	0.09	1.25 ± 3.04
Cloud H						
H1	1.5	0.27 ± 0.03	45.09 ± 0.10	1.89 ± 0.28	0.13	4.87 ± 2.44
H2	1.5	0.26 ± 0.03	45.47 ± 0.08	1.62 ± 0.32	0.15	1.38 ± 1.44
H3	1.5	0.50 ± 0.05	45.41 ± 0.23	5.13 ± 0.63	0.09	0.10 ± 3.98
H4	1.6	0.23 ± 0.02	45.51 ± 0.08	1.57 ± 0.18	0.14	0.81 ± 1.43
H5	1.5	0.31 ± 0.03	45.43 ± 0.10	2.06 ± 0.24	0.14	0.56 ± 1.69
H6	2.8	0.26 ± 0.03	45.37 ± 0.06	0.74 ± 0.22	0.33	0.10 ± 1.58

Notes. (*) Indicates 3σ upper-limit values for $T_{\rm peak}$. ≤ on the integrated intensity $\int T_{\rm mb}\ \Delta\upsilon$ indicates the upper limits which are calculated as $3\sigma \times \sqrt{\delta\upsilon \times \Delta\upsilon}$ with $\delta\upsilon$ the spectral resolution (0.68 km s^{-1}) and $\Delta\upsilon$ the average line width measured considering all cores.

Table A.5. Root mean square noise in the spectra rms, integrated intensities $\int T_{\rm mb} {\rm d}\upsilon$, radial velocity υ, line widths $\Delta\upsilon$, peak temperature $T_{\rm peak}$ of the HCN ($1 \rightarrow 0$, $F = 2 \rightarrow 1$) hyperfine component and optical depth τ of the HCN(1→0) emission in cores within Clouds G and H.

Core	rms [10^{-2} K]	$\int T_{\rm mb}\Delta\upsilon$ [K km s^{-1}]	υ [km s^{-1}]	$\Delta\upsilon$ [km s^{-1}]	$T_{\rm peak}$ [K]	τ
Cloud G						
G1	1.4	0.95 ± 0.07	42.66 ± 0.16	4.05 ± 0.31	0.22	0.10 ± 0.16
G3	2.3	1.03 ± 0.05	40.43 ± 0.05	1.17 ± 0.09	0.82	0.10 ± 0.02
Cloud H						
H2	1.6	3.32 ± 0.05	44.06 ± 0.02	3.19 ± 0.05	0.98	1.29 ± 0.18
H3	1.4	4.71 ± 0.06	43.80 ± 0.02	3.48 ± 0.05	1.27	1.16 ± 0.13
H4	1.5	3.26 ± 0.06	44.47 ± 0.03	3.34 ± 0.07	0.92	0.71 ± 0.04
H5	2.0	3.32 ± 0.05	44.43 ± 0.04	3.36 ± 0.06	0.93	1.84 ± 0.29